JOURNAL OF SOLID STATE CHEMISTRY **130,** 223–233 (1997)
ARTICLE NO. SC977294

Effect of Iron Substitution on the Structural, Electric, and Magnetic Properties in *R*-Type $PbFe_xV_{6-x}O_{11}$, a Frustrated System

Olivier Mentre, Anne-Claire Dhaussy, and Francis Abraham[1]

Laboratoire de Cristallochimie et Physicochimie du Solide, URA CNRS 452, ENSCL, Universite des Sciences et Technologies de Lille, BP 108, 59652 Villeneuve d'Ascq Cedex, France

and

Hugo Steinfink

Center of Materials Science and Engineering, Department of Chemical Engineering, University of Texas at Austin, Austin, Texas 78712-1063

Received September 23, 1996; in revised form January 17, 1997; accepted January 27, 1997

Single-phase material of the solid solution $PbFe_xV_{6-x}O_{11}$ was prepared by solid-state reaction over the range $1 \leq x \leq 1.75$. Powder preparations of PbV_6O_{11}, however, were always accompanied by a small amount of impurity. The noncentrosymmetric space group $P6_3mc$ of PbV_6O_{11}, which has an *R*-block structure, remains unchanged with iron substitution. The crystal structure of $PbFe_{1.75}V_{4.25}O_{11}$ was refined from single-crystal X-ray data to $R = 0.049$. The iron atoms are located preferentially in specific crystallographic sites. The triangular–bipyramidal site is completely occupied by Fe^{3+} while the interstices of the central octahedral layer are solely occupied by the vanadium V(1) atoms. The other two crystallographic sites have mixed Fe/V occupancies. Magnetic measurements performed on nearly single-phase PbV_6O_{11} and the iron substituted phases reveal a spin-glass-type behavior with freezing temperatures T_f of 50 and 65 K, respectively. T_f is independent of the iron ratio. This spin-disordered system is attributed to strong frustration occurring in the *a–b* plane because of the existence of V(1) trimers providing alternatively long and short V–V distances along the *a* axis. Resistance and Seebeck coefficient measurements indicate *p*-type conduction above T_f while the system becomes an insulator below T_f. Fe^{3+} ions do not participate in the hopping process, and they block conduction parallel to the *c* axis because of their location in the bridging dimeric octahedral and bipyramidal sites.

1. INTRODUCTION

Recently, Mentre and Abraham described the crystal structure of PbV_6O_{11} (1), a new lead mixed valence vanadium V^{3+}–V^{4+} oxide. This compound belongs to the well-known *R*-hexagonal ferrite family. Its structure is closely related to the magnetoplumbite $PbFe_{12}O_{19}$ and $BaFe_{12}O_{19}$ (2, 3). They consist of the packing along the *c* axis of *R* blocks and *S* spinel blocks (2, 3). *R* blocks were first isolated in $BaFe_4Te_2O_{11}$ with space group $P6_3/mmc$ at room temperature (4). The same space group is found at room temperature for all other AV_6O_{11} compounds investigated to date (5). In PbV_6O_{11}, the Pb^{2+} $6s^2$ lone pair gives rise to the noncentrosymmetric $P6_3mc$ space group. This oxide is isostructural with the low temperature, 200 K, form of NaV_6O_{11} (6).

In addition to the interesting behavior of V^{3+}–V^{4+} mixed-valence 3*d* electrons, which may be in an intermediate state between localized and itinerant as in the perovskite $La_{1-x}Sr_xVO_3$ or the spinel $Zn_{1-x}Li_xV_2O_4$ systems (7, 8), the coupling of magnetic moments among ions within and between *R* blocks is of great interest. The magnetic exchange interactions may vary from classical parallel spin alignments to disordered spin-glass systems. Correlations between magnetic and transport properties have been reported for AV_6O_{11}, A = Na, Sr, and reveal completely different phenomena depending on the nature of the *A* ion (6, 9).

Many unsuccessful attempts were made to grow sufficiently big single crystals or single-phase powder of lead vanadium oxide in order to investigate its properties (1). The best polycrystalline samples of almost single-phase PbV_6O_{11} always contained a small amount of lead vanadium hollandite, $Pb_{1.32}V_{8.35}O_{16.7}$, which is stoichiometrically close to the desired phase. Previously reported syntheses of $SrT_xV_{6-x}O_{11}$ ($T = Ti^{4+}$, Cr^{3+}, and Fe^{3+}) solid solutions (10) provide clues for the synthesis of pure $PbT_xV_{6-x}O_{11}$. We prepared such powders with T = Fe in the $1 \leq x \leq 1.75$ domain. This paper reports the crystal structure of $PbFe_{1.75}V_{4.25}O_{11}$ and the effects of the

[1] To whom correspondence should be addressed.

0022-4596/97 $25.00

substitution of V^{3+} by Fe^{3+} on the structural, magnetic, and electric properties.

EXPERIMENTAL

Synthesis

$Pb_2V_2O_7$ was obtained by heating a 2:1 molar ratio of PbO and V_2O_5 at 600°C in air for three days, V_2O_3 was obtained by reducing V_2O_5 under flowing hydrogen at 850°C. The starting materials $Pb_2V_2O_7$, Fe_2O_3, and V_2O_3 were mixed in a $1/2 : x/2 : (5 - x)/2$ molar ratio, introduced into a gold tube that was sealed in an evacuated silica tube, and then heated at 850°C for three days. Composition in the $0.5 \leq x \leq 2.5$ range were synthesized. X-ray powder diffraction patterns were obtained with a Siemens D5000 diffractometer equipped with a graphite crystal diffracted-beam monochromator and Cu$K\alpha$ radiation. Single phases existed for the compositions $1 \leq x \leq 1.75$ as shown by the match of their powder X-ray diffraction patterns with that reported for PbV_6O_{11} (1). Compositions corresponding to the smallest values of x were accompanied by Pb–V hollandite as an impurity while greater values of x showed the presence of Fe_2O_3 in the product. Figure 1 shows the X-ray powder diffraction pattern obtained for pure $PbFe_{1.75}V_{4.25}O_{11}$ compared to a $PbV_6O_{11}/Pb_{1.32}V_{8.35}O_{16.7}$ mixture that was often obtained in our previous preparations (1). Figure 2 is a plot of the unit-cell parameters obtained from a least-squares refinement of the powder data for the four compositions $x = 1, 1.25, 1.5, 1.75$. The a parameter of the hexagonal cell is nearly constant while c increases linearly with x.

Attempts to substitute Ti^{4+} and Cr^{3+} for V^{4+} and V^{3+} failed. They lead to the formation of Pb–V hollandite that is the predominant component in a mixture of otherwise unidentified phases. Moreover, Kanke *et al.* found that only Sr is an acceptable A cation in AT_6O_{11}-type compounds among various divalent or trivalent metals such as Ca, Ba, La, and Nd (10). Our attempts to prepare AV_6O_{11} with $A = Bi^{3+}$ and Tl^{+} failed.

Single-Crystal X-Ray Analysis

Single crystals corresponding to the $x = 1.75$ composition were prepared from the stoichiometric mixture of oxides contained in a gold tube that was sealed into a silica tube evacuated to about 10^{-3} Torr. The tube was heated at 950°C for five days. After cooling, a black hexagonal platelet 18 μm in thickness was isolated from the homogeneous product and mounted on a glass fiber. EDS (energy dispersive spectroscopy) microprobe elemental analysis was performed on the single crystal with a Philips 525M scanning electron microscope connected to an Edax PV9900 analyzer. The atomic ratio Pb : Fe : V = 1 : 1.80 : 4.31 is in good agreement with the expected formula.

Parameters of the unit cell $a = 5.74$ Å and $c = 13.50$ Å, Laue symmetry $6/mmm$ and absences of $hh(2h)l$ reflections

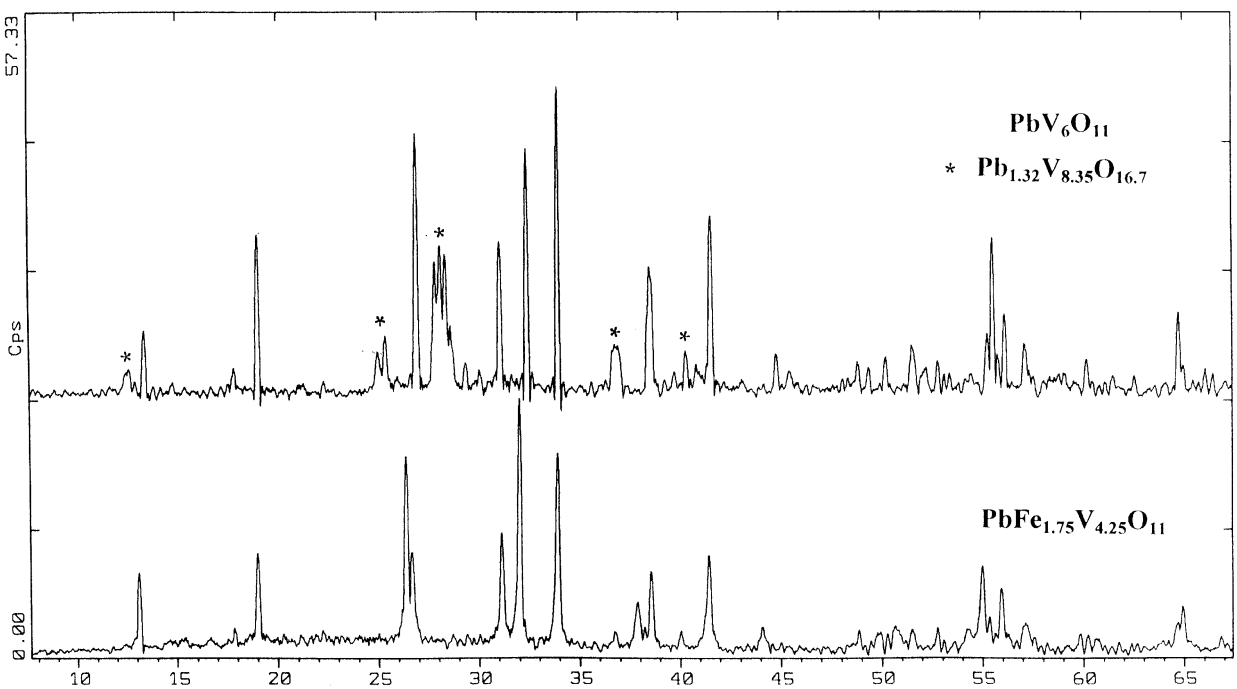

FIG. 1. X-ray diffraction powder pattern of $PbV_6O_{11}/Pb_{1.32}V_{8.35}O_{16.7}$ mixed and single-phase $PbFe_{1.75}V_{4.25}O_{11}$.

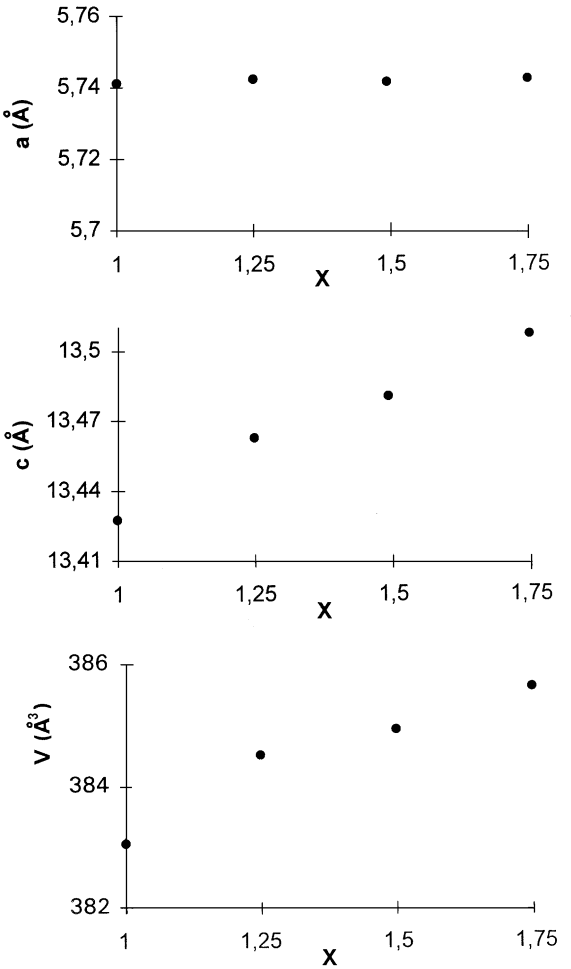

FIG. 2. Lattice parameters a, c, and volume of the hexagonal unit-cell for $PbFe_xV_{6-x}O_{11}$ phases vs composition.

TABLE 1
Crystal Data, Intensity Measurement, and Structure Refinement Parameters for $PbFe_{1.75}V_{4.25}O_{11}$

Crystal Data	
Crystal symmetry	Hexagonal
Space group	$P6_3mc$
Cell dimension (Å)	$a = 5.742(2)$, $c = 13.507(5)$
Volume (Å^3)	385.2
Z	2
Data Collection	
Equipment	Philips PW 1100
λ (Mo$K\alpha$ (graphite monochromator))	0.7107 Å
Scan mode	ω-2θ
Scan width (°)	1.8
θ range (°)	2–35
Standard reflections measured every 2 h (no decay)	112, 210, 120
Recording reciprocal space	$-9 \le h \le 9$, $-9 \le k \le 9$, $0 \le 1 \le 21$
Number of measured reflections	3451
Number of reflections $I < 3\sigma(I)$	2478
Number of independent reflections	324
μ (cm^{-1}) (for λ $K\alpha = 0.7107$ Å)	300.09
Limiting faces and distances (mm) from arbitrary origin	001 0.01 00$\bar{1}$ 100 0.045 $\bar{1}$00 010 0.035 0$\bar{1}$0 1$\bar{1}$0 0.05 $\bar{1}$10
Transmission factor range	0.16–0.58
Merging R factor	0.049
Refinement	
Number of refined parameters	40
$R = \sum[F_o - F_c]/\sum F_o$	0.049
$R_w = [\sum w(F_o - F_c)^2/\sum wF_o^2]^{1/2}$	0.040
With $w = 1/\sigma(F_o)$	

$l = 2n + 1$, are consistent with three possible space groups $P6_3mc$, $P6_3/mmc$, and $P\bar{6}2c$ and point to an R-type ferrite structure. Half of reciprocal space was recorded with a Philips PW1100 diffractometer. Data collection parameters are reported in Table 1. Intensities were corrected for Lorentz-polarization effects. Absorption corrections were applied using the analytical method of De Meulenaer and Tompa (11) with $\mu = 300.09\ cm^{-1}$ corresponding to the predicted stoichiometry. Structural refinement was performed in the three possible space groups but as in the PbV_6O_{11} case, only the noncentrosymmetric $P6_3mc$ space group allowed the refinement to converge, providing the lowest reliability factors and reasonable interatomic distances. The atomic scattering factors for neutral atoms were taken from "International Tables for X-Ray Crystallography" (12) and values for the anomalous dispersion correction from Cromer and Liberman (13). The full-matrix least-squares refinement was performed with a local modification of the SFLS-5 program (14).

Patterson functions showed the location of Pb atoms in 2(*b*) $(1/3, 2/3, z;\ 2/3, 1/3, 1/2 + z)$ confirming the isomorphism of the substituted phases with PbV_6O_{11}. Transition metal and oxygen atoms were subsequently located by the calculation of Fourier difference syntheses. The use of all atomic positional and isotropic displacement parameters in the least-squares refinement yielded $R = 0.062$ and $R_w = 0.071$. At this stage, all the transition metal atoms had been considered as vanadium. Maxima appearing in two of the 2(*a*) and one 2(*b*) special positions in the subsequent Fourier difference maps were assigned to mixed Fe/V sites. The ratios were chosen on the basis of peak heights and stoichiometry and thereafter held fixed. Moreover, the negative value of the isotropic B factor for the statistical atom in the triangular bipyramidal 2(*b*) site made it an excellent candidate for a fully occupied iron position. In the last least-squares refinement cycle the atomic positional and occupancy parameters of Table 2, anisotropic displacements and secondary extinction parameters and a weighting

TABLE 2
(a) Atomic Coordinates and Isotropic Displacement Parameters, Å², for $PbFe_{1.75}V_{4.25}O_{11}$

Atom	Site	Occupancy	x	y	z	B_{eq} (Å²)*
Pb	2*b*	1	1/3	2/3	0.2214(8)	1.22(1)
V(1)	6*c*	1	0.5094(2)	− 0.5094	− 0.0003(8)	0.38(3)
M(2) [V/Fe]	2*a*	0,75/0,25	0	0	0.1459(9)	0.15(9)
M(3) [V/Fe]	2*a*	0,5/0,5	0	0	0.3522(9)	0.40(9)
Fe(4)	2*b*	1	2/3	1/3	0.2703(9)	1.51(9)
O(1)	6*c*	1	0.173(1)	− 0.173	0.081(1)	0.7(2)
O(2)	6*c*	1	0.153(1)	− 0.153	3/4	0.7(2)
O(3)	6*c*	1	0.173(1)	− 0.173	0.421(1)	0.9(3)
O(4)	2*b*	1	2/3	1/3	0.420(2)	0.4(3)
O(5)	2*b*	1	2/3	1/3	0.086(2)	1.0(4)

(b) Anisotropic Thermal Parameters of $PbFe_{1.75}V_{4.25}O_{11}$

Atom	U_{11}	U_{22}	U_{33}	U_{12}	U_{13}	U_{23}
Pb	0.0162(3)	$= U_{11}$	0.0140(4)	$= U_{11}/2$	0	0
V(1)	0.0085(10)	$= U_{11}$	0.0407(32)	$= U_{11}/2$	0	0
M(2) [V/Fe]	0.0002(13)	$= U_{11}$	0.0055(23)	$= U_{11}/2$	0	0
M(3) [V/Fe]	0.0048(5)	$= U_{11}$	0.0029(8)	0.0012(7)	0.0015(6)	$= -U_{13}$
Fe(4)	0.0072(16)	$= U_{11}$	0.0010(21)	$= U_{11}/2$	0	0

* B_{eq} is defined as $4/3 \sum_i \sum_j \beta_{ij} a_i a_j$.
U_{ij} is defined as $\exp[-2\pi^2(U_{11}h^2a^{*2} + \ldots + 2U_{23}klb^*c^*)]$.

scheme were introduced, yielding $R = 0.049$ and $R_w = 0.040$. Interatomic distances and angles are reported and compared with those of PbV_6O_{11} in Table 3.

Magnetic and Electric Properties Measurements

Magnetic susceptibilities were measured with a quantum Design DC SQUID magnetometer over the range 10–300 K. Zero-field-cooling (ZFC) and field-cooling (FC) data were measured with different applied fields depending on the sample. DC resistance measurements were performed on sintered powder pellets with a standard four-probe method using instruments with IEEE-488 interfaces and an IBM P-512 computer as a controller. Data were collected from room temperature to 5 K on cooling. The DC current applied between the two external probes was 10 mA. Thermoelectric-power measurements were made with a Keithley 181 nanovoltmeter at stable temperatures, T_1 and T_2, generated across the disk with $\Delta T = 4$ K. The results were collected from high temperature to helium temperature in three different ranges corresponding to 10–80 K, 80–310 K, and 310–600 K.

DISCUSSION

Structural Features

The structure of $PbFe_{1.75}V_{4.25}O_{11}$ differs from that of PbV_6O_{11} because of the statistical occupancy of selected crystallographic sites and the distortion of some polyhedra. Figure 3 shows the crystal structure and atom labels. The interstices of the central octahedral layer retain the V(1) occupancy to form a Kagome type lattice, but the interstices of the dimeric, face sharing octahedra that connect on each side by corner sharing to the central octahedral layer are occupied by the *M*(2), V : Fe = 3 : 1, and *M*(3), V : Fe = 1 : 1, ions. The trigonal bipyramids that connect pairs of dimeric octahedra are occupied solely by Fe^{3+}(4). The Pb^{2+} ions occupy cuboctahedral interstices that exist in the Pb–Fe(4)–O(2) layers (see Fig. 4).

The different sites occupancies for mixed-cationic compounds and valences for vanadium phases in the various crystallographic sites are shown in Table 4 for several *R*-block compounds. For each compound, the metal–oxygen distances for the triangular bipyramidal site are also shown. PbV_6O_{11} exhibits asymmetry in the 2(*b*) site due to the Pb^{2+} $6s^2$ lone pair effect so that Pb^{2+} is displaced 0.35 Å parallel to the *c* axis from the pseudo-mirror plane containing the O(2) atoms. The V^{4+} ion in the bipyramidal interstice moves 0.17 Å along the *c* axis in the opposite direction. This decreases the electrostatic repulsion between the cations and imparts a slight tetrahedral character to the trigonal bipyramid. In $PbFe_{1.75}V_{4.25}O_{11}$ the Pb atom is located 0.38 Å on one side of the oxygen plane while Fe^{3+} is shifted 0.27 Å on the other side (see Fig. 4). The substitution of V^{4+} by Fe^{3+} exaggerates the displacement because of the inherent tetrahedral site preference of Fe^{3+}. The three short

TABLE 3
Interatomic Distances[a] (Å) and Selected Bond Angles (°) for $PbFe_{1.75}V_{4.25}O_{11}$ and PbV_6O_{11} (PbV_6O_{11} Shown in Italics)

V(1) octahedron		Angles	
$2\times V(1)$–$O(1)^{ii,iii}$:	2.006(10) *1.983(9)*	$1\times O(1)^{ii}$–V(1)–$O(1)^{iii}$:	87.0(6) *86.1(5)*
$2\times V(1)$–$O(3)^{v,vi}$:	1.904(11) *1.913(9)*	$1\times O(3)^{v}$–V(1)–$O(3)^{vi}$:	93.0(5) *93.9(4)*
$1\times V(1)$–$O(4)^{iv}$:	2.056(15) *2.114(9)*	$1\times O(4)^{iv}$–V(1)–$O(5)^{i}$:	175(10) *174(6)*
$1\times V(1)$–$O(1)^{i}$:	1.951(17) *1.998(10)*	$2\times O(1)^{ii}$–V(1)–$O(4)^{iv}$:	83(1) *82.6(6)*
		$2\times O(1)^{ii}$–V(1)–$O(5)^{i}$:	93.1(7) *84.8(2)*
		$2\times O(1)^{ii}$–V(1)–$O(3)^{vi}$:	89.8(8) *89.6(7)*
		$2\times O(1)^{ii}$–V(1)–$O(3)^{v}$:	175(7) *173(5)*
V(1)–$O(1)^{iii}$–V(1):	98.2(5) *101.4(5)*	$2\times O(3)^{v}$–V(1)–$O(4)^{iv}$:	92.9(6) *91.1(4)*
V(1)–$O(4)^{iv}$–$V(1)^{iii}$:	95.1(6) *93.1(3)*	$2\times O(3)^{v}$–V(1)–$O(5)^{i}$:	90(1) *93.1(7)*
M(2) octahedron		Angles	
$3\times M(2)$–$O(1)^{i,ii,iii}$:	1.931(10) *1.971(9)*	$3\times O(1)^{i}$–*M*(2)–$O(1)^{ii}$:	101.0(8) *101.2(7)*
$3\times M(2)$–$O(2)^{iv,v,vi}$:	2.072(10) *2.053(8)*	$3\times O(2)^{iv}$–*M*(2)–$O(2)^{v}$:	79.0(3) *78.8(3)*
		$3\times O(1)^{i}$–*M*(2)–$O(2)^{iv}$:	164(3) *164(3)*
		$6\times O(1)^{i}$–*M*(2)–$O(2)^{v}$:	88.9(6) *88.9(5)*
M(3) octahedron		Angles	
$3\times M(3)$–$O(2)^{iv,v,vi}$:	2.055(10) *2.007(8)*	$3\times O(2)^{iv}$–*M*(3)–$O(2)^{v}$:	79.8(3) *81.0(3)*
$3\times M(3)$–$O(3)^{i,ii,iii}$:	1.9555(11) *1.924(9)*	$3\times O(3)^{i}$–*M*(3)–$O(3)^{ii}$:	99.3(8) *100.4(4)*
		$3\times O(2)^{iv}$–*M*(3)–$O(3)^{i}$:	166(3) *166(3)*
		$6\times O(2)^{iv}$–*M*(3)–$O(3)^{ii}$:	89.6(6) *88.4(6)*
Fe(4) trigonal bipyramid		Angles	
$3\times Fe(4)$–$O(2)^{iv,v,vi}$:	1.814(7) *1.826(7)*	$3\times O(2)^{iv}$–Fe(4)–$O(2)^{v}$:	117.7(6) *119.1(6)*
$1\times Fe(4)$–$O(4)^{i}$:	2.022(30) *1.960(16)*	$1\times O(4)^{i}$–Fe(4)–$O(5)^{i}$:	180 *180*
$1\times Fe(4)$–$O(5)^{i}$:	2.489(30) *2.259(16)*	$3\times O(2)^{iv}$–Fe(4)–$O(4)^{i}$:	98(1) *95.5(8)*
		$3\times O(2)^{iv}$–Fe(4)–$O(5)^{i}$:	81(1) *84.4(6)*
Pb cuboctahedron		Cation–cation	
$3\times Pb$–$O(1)^{i,ii,iii}$:	2.478(14) *2.485(12)*	$2\times V(1)$–$V(1)^{ii}$:	2.709(2) *2.684(2)*
$6\times Pb$–$O(4)^{iv,v,vi}$:	2.900(4) *2.903(4)*	$2\times V(1)$–$V(1)^{ii}$:	3.033(2) *3.070(2)*
$3\times Pb$–$O(5)^{i,ii,iii}$:	3.132(15) *3.036(13)*	$1\times M(2)$–$M(3)^{i}$:	2.786(17) *2.725(13)*
		$3\times Pb$–$M(2)^{i}$:	3.469(5) *3.481(4)*
		$3\times Pb$–$M(3)^{i}$:	3.757(8) *3.725(6)*

[a] Symmety cards: i: x, y, z; ii: $\bar{y}, x-y, z$; iii: $\bar{x}+y, \bar{x}, z$; iv: $\bar{x}, \bar{y}, z+1/2$; v: $y, \bar{x}+y, z+1/2$; vi: $x-y, x, z+1/2$.

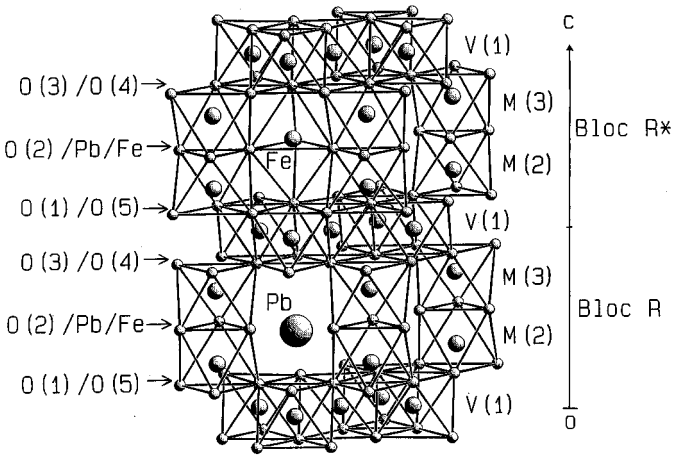

FIG. 3. Crystal structure of the *R* block of $PbFe_{1.75}V_{4.25}O_{11}$.

equatorial bonds, Fe–O(2) = 1.824(5) Å, are nearly equal to the corresponding V–O(2) = 1.826(7) Å bonds. However, the two apical distances, Fe–O(5) = 2.49(3) Å and Fe–O(4) = 2.02(3) Å, are considerably longer than the V–O(5) = 2.259(16) Å and V–O(4) = 1.960(16) Å bonds. The decrease in these V^{4+}–O apical bonds is due to the much stronger interaction of the oxygen *s*–*p* orbitals with the *d* manifold of a d^1 ion than a d^5 ion. This shortening of the apical V–O bond compared to Fe–O bonds has been noticed for many compounds as shown in Table 4.

The lengthening of the apical distances explains the increase of the *c* parameter versus *x* shown in Fig. 2. The difference in the *c* parameters for $PbFe_{1.75}V_{4.25}O_{11}$ and PbV_6O_{11} is 0.24 Å. The differences of the heights of the bipyramids in the two phases parallel to the *c* axis is about 0.30 or 0.60 Å per unit cell. The height of the central octahedral layer occupied by V(1) in both compounds must, therefore, be less in $PbFe_{1.75}V_{4.25}O_{11}$ than in PbV_6O_{11}. The observed decrease is 0.18 Å, or 0.36 Å per unit cell, in agreement with the observed difference in the *c* axes. A similar *c* evolution has been noticed for $SrFe_xV_{6-x}O_{11}$ (10).

It is instructive to examine the cation distributions in the related structures $SrT_xV_{6-x}O_{11}$, T = Ti, Cr, Fe, determined by the Rietveld refinement of their neutron powder pattern by Kanke *et al.* (10). The central octahedral interstices of investigated $Ti_1, Ti_{1.5}, Cr_1$, and Fe_1 phases contain about 14% of the substituents Ti and Cr but no Fe, which is in agreement with the V only occupancy of this site in $PbFe_{1.75}V_{4.25}O_{11}$. The interstices of the dimeric octahedral units *M*(2) contain about 24% of the substituents except for the $Ti_{1.5}$ phase that contains 39% Ti. Pronounced differences in the site occupancies occur in the bipyramidal sites *M*(4): 16 and 35% Ti, respectively, in the $x = 1$ and 1.5 phases; 7% in the Cr phase; 56% Fe in the $x = 1$ phase.

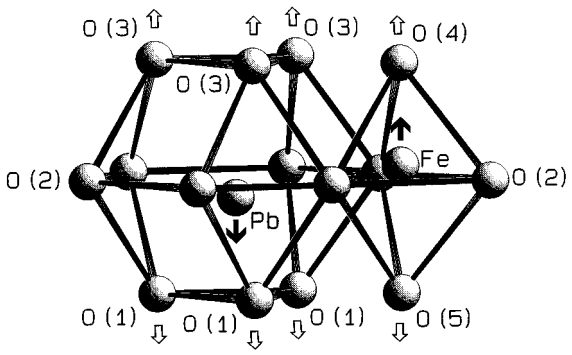

FIG. 4. Fe/V triangular-bipyramid and Pb cuboctahedron in $PbFe_{1.75}V_{4.25}O_{11}$. The arrows represent the displacement of the atoms as compared to PbV_6O_{11}.

TABLE 4
Site Occupancy for Mixed *R*-Type Compounds, Valency for Vanadium *R*-Type Compounds and Trigonal Bipyramid *M*(4)–O Distances (Å) in Several Oxides

	$BaTi_2Fe_4O_{11}$[a]	$BaSn_2Fe_4O_{11}$[a]	$SrTiV_5O_{11}$[b]	$SrTi_{1.5}V_{4.5}O_{11}$[b]	$SrCrV_5O_{11}$[b]
M(1)	65%Fe, 35%Ti	74%Fe, 26%Sn	12%Ti, 88%V	13%Ti, 87%V	15%Cr, 85%V
M(2)	52%Fe, 48%Ti	39%Fe, 61%Sn	24%Ti, 76%V	39%Ti, 61%V	23%Cr, 77%V
M(3)	—	—	—	—	—
M(4)	100%Fe	100%Fe	16%Ti, 84%V	35%Ti, 65%V	7%Cr, 93%V
$3 \times M(4)$–O(2)	1.867(5)	1.907(5)	1.808(4)	1.818(6)	1.787(4)
$1 \times M(4)$–O(4)	2.098(14)	2.044(10)	2.110(4)	2.124(8)	2.071(4)
$1 \times M(4)$–O(5)	2.583(14)	2.603(10)	2.110(4)	2.124(8)	2.071(4)
	$SrFeV_5O_{11}$[b]	$PbFe_{1.75}V_{4.25}O_{11}$	PbV_6O_{11}	SrV_6O_{11}[c]	NaV_6O_{11}[c]
M(1)	100%V	100%V	V^{3+}	V^{3+}	V^{3+}
M(2)	24%Fe, 76%V	25%Fe, 75%V	V^{3+}	V^{4+}	V^{4+}
M(3)	—	50%Fe, 50%V	V^{4+}	—	—
M(4)	56%Fe, 44%V	100%Fe	V^{4+}	V^{3+}	V^{4+}
$3 \times M(4)$–O(2)	1.817(4)	1.814(7)	1.826(7)	1.832(6)	1.7869(6)
$1 \times M(4)$–O(4)	1.867(9)	2.022(30)	1.960(16)	2.11(1)	2.086(1)
$1 \times M(4)$–O(5)	2.339(9)	2.489(30)	2.259(16)	2.11(1)	2.086(1)

[a] From Ref. (15).
[b] From Ref. (5), *M*(4)–O distances for $SrFeV_5O_{11}$ compound are given for iron location in that site.
[c] From Ref. (6).

Evidently Fe^{3+} strongly prefers the bipyramidal site, and we suggest that in $SrFe_{1.75}V_{4.25}O_{11}$ this site would solely contain Fe in agreement with the result for $PbFe_{1.75}V_{4.25}O_{11}$. Similar results are also seen in the structures for $BaTi_2Fe_4O_{11}$ and $BaSn_2Fe_4O_{11}$ (4, 15). In both compounds the bipyramidal site is occupied only by Fe^{3+} that is displaced from the equatorial oxygen triangle in accord with its strong preference for a tetrahedral environment.

Magnetic Properties

Magnetic properties of hexagonal *R*-block ferrite-type compounds depend on competing exchange interactions. The ferrimagnetism of $BaTi_2Fe_4O_{11}$ (16) and the ferromagnetism of NaV_6O_{11} (9) are due to collinear coupling of spins. The isomorphous replacement of the metallic cations by different elements can introduce disordered magnetic interactions. Thus, quasi-two-dimensional, strongly fluctuating spins in highly frustrated systems (17–19), local, random-spin canting, (20), and spin-glass behavior (21–23), have been reported. There are basically two different possible interpretations of such a disordered state. The first case assumes a true phase transition. In that case, individual canted, ferro- and antiferromagnetic exchange coupling modes interact below the freezing temperature T_f to give rise to a true equilibrium phase as described for a canonical spin glass. The *R*-block structure $BaSn_xTi_{2-x}Fe_4O_{11}$ and the *RS*-block structure $BaCo_6Ti_6O_{19}$ exhibit such a behavior (21, 22). In the second case, the spin glass is considered to arise from a superparamagentic set of differently sized clusters of spins. *R*-type $BaFe_{2.8}Sn_{3.1}Co_{1.1}O_{11}$ exhibits this type of behavior because of the occupancy of the 4(*e*) dimer positions by a d^{10} Sn^{4+} ion, weakening the magnetic exchange parallel to the *c* axis and forming Fe–Co octahedral layers of spins (23).

In Figs. 5a and 5b, the zero field cooled (ZFC) and field cooled (FC) measurements for PbV_6O_{11} and $PbFe_{1.75}V_{4.25}O_{11}$ in applied fields of 1000 Oe for the former and 100 Oe for the latter phase are shown. The initial negative values of χ for $PbFe_{1.75}V_{4.25}O_{11}$ are due a remanent magnetic field trapped in the superconducting coil of the SQUID at the beginning of the experiment. The magnetic behavior for both isostructural phases is the same and is consistent with the formation of a disordered spin structure at low temperature. The ZFC and FC measurements begin to diverge at about 120 K for PbV_6O_{11} and a peak is present at about 50 K in the ZFC data corresponding to the freezing temperature, T_f. The same features are observed for the susceptibility data for $PbFe_{1.75}V_{4.25}O_{11}$ but the divergence occurs at about 175 K and T_f is about 65 K. The difference observed in the χ data for PbV_6O_{11} in the paramagnetic region, Fig. 5a, is very small and becomes greatly exagereted in the χ^{-1} plot. The divergence is probably due to the gradual rearrangement of Weiss domains during the measurements. We assume that this does not affect sensitively the low temperature χ results. Figure 6 shows the hysteresis cycle obtained for $PbFe_{1.75}V_{4.25}O_{11}$ at 30 K. The remanent magnetic moment is 1000 emu/mol and the coercitive field is

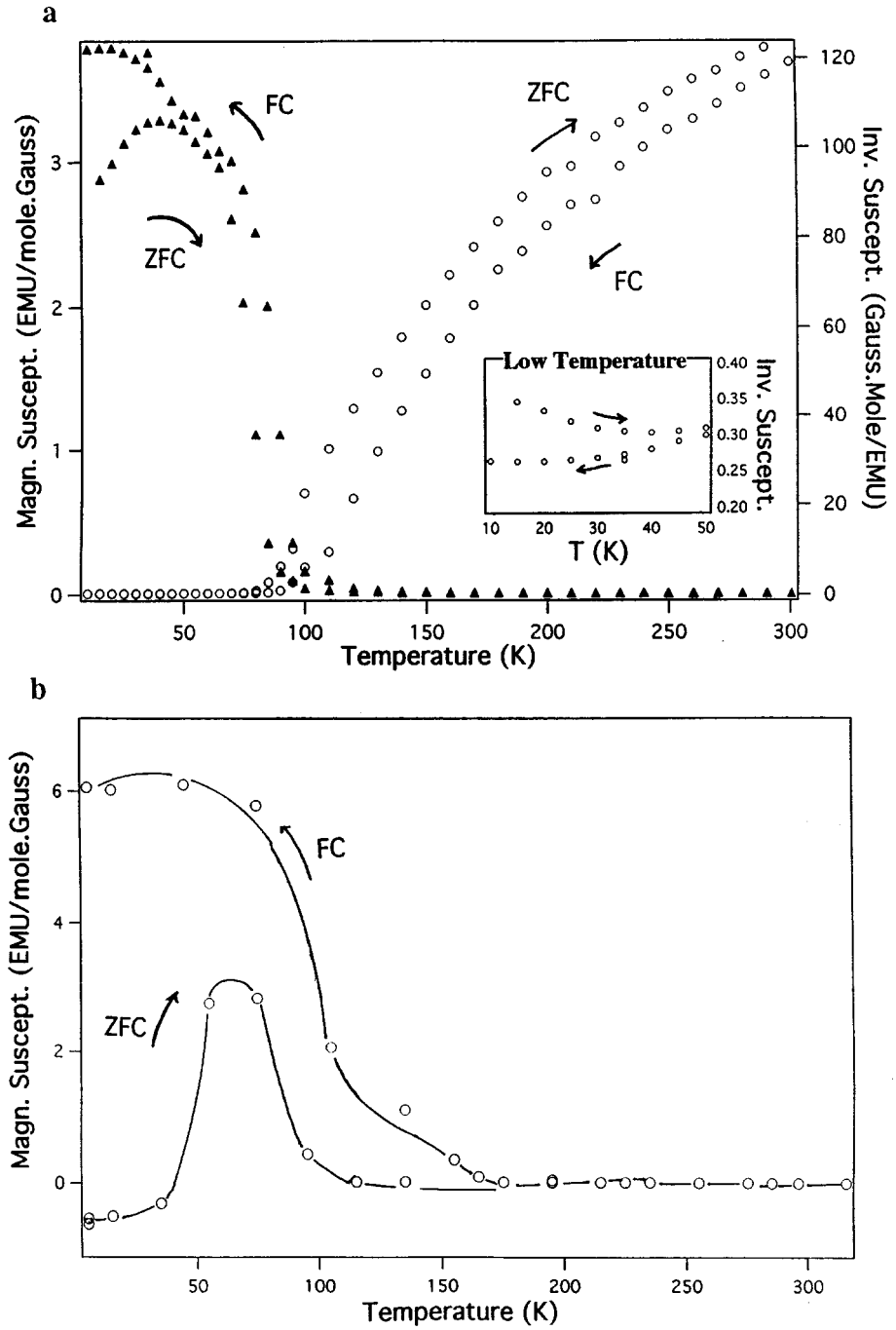

FIG. 5. Thermal dependence of (a) susceptibility (filled triangles) and inverse susceptibility (open circles) for PbV_6O_{11}. (b) Susceptibility for $PbFe_{1.75}V_{4.25}O_{11}$.

1000 Gauss. The symmetrical shape of the loop suggests a spin-frustration model rather than a spin-glass system. Saturation is not achieved at 1000 G, and the fields used in these measurements are too small to cause deviations from a linear M vs H relationship in the measurements of the susceptibility, especially in the paramagnetic region.

The interstices of the central octahedral layer are occupied by V(1) forming a hexagon in the a–b plane. The V(1) ions are displaced from the centers of the octahedra in the 6(c) site of $P6_3mc$ and form two sets of triangles sharing corners. The smaller triangle of PbV_6O_{11} is formed by a V(1)–V(1) = 2.684(2) Å distance and the larger by the

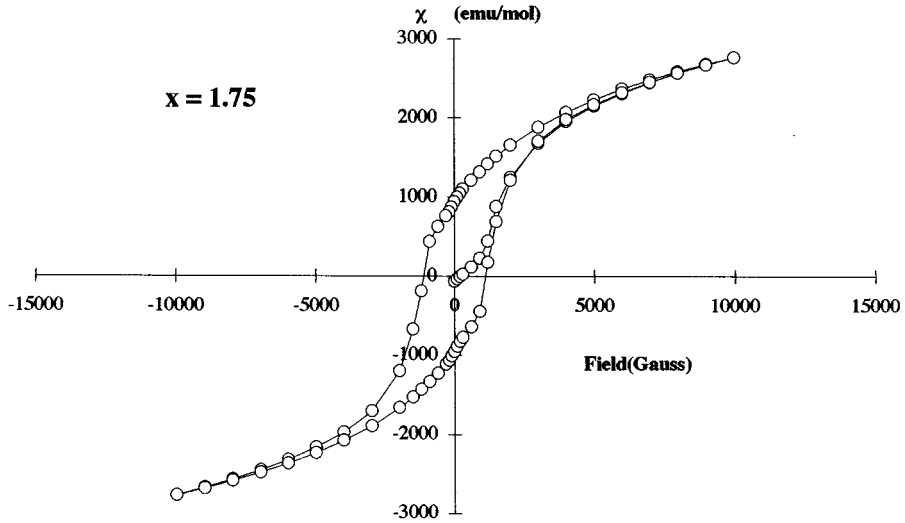

FIG. 6. χ vs H hysteresis cycle at 30 K for $PbFe_{1.75}V_{4.25}O_{11}$.

3.070(2) Å distance. A similar distortion exists in monoclinic VO_2 leading to bonded and nonbonded V–V with the same distances. In contrast, ferromagnetic NaV_6O_{11} and ferro/ferri magnetic SrV_6O_{11} exhibit only one kind of triangle at room temperature with V(1)–V(1) = 2.885 and 2.856 Å, respectively. Manthiram and Goodenough determined a critical V–V separation, R_c, for direct metal–metal magnetic interaction in oxides as 2.89 Å $< R_c <$ 2.97 Å and narrowed it to the range 2.89 Å $< R_c <$ 2.93 Å in the case of localized V^{3+} cations (24), as in the PbV_6O_{11} a–b layers. Thus, direct exchange between the short V(1)–V(1) bonds gives rise to ferromagnetic coupling as in NaV_6O_{11}, while superexchange paths via oxygen p^6 orbitals of the O(4) and O(1) atoms exists between the long V(1)–V(1) bonds. V(1)–O(4)–V(1) and V(1)–O(1)–V(1) angles are close to 90° (93.1°(4) and 101.4°(5), respectively) and give rise to antiferromagnetic exchange (25). This triangular spin arrangement leads to frustration in the a–b plane (and the formation of a spin-glass-type compound) below T_f (26). A possible low-energy model of spin couplings in the sheets showing V–V and V–O–V interactions is presented in the Fig. 7. The substitution of high-spin Fe^{3+} cations occurs only in the $M(2)$, $M(3)$, and $M(4)$ sites and does not affect the freezing temperature (see Fig. 8), which is in agreement with the

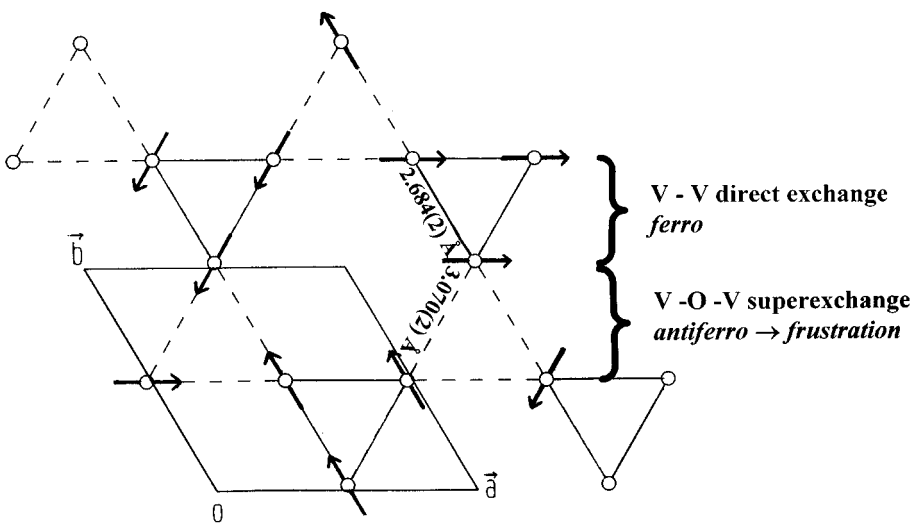

FIG. 7. Low energy spin arrangement arising in the a–b octahedral layers.

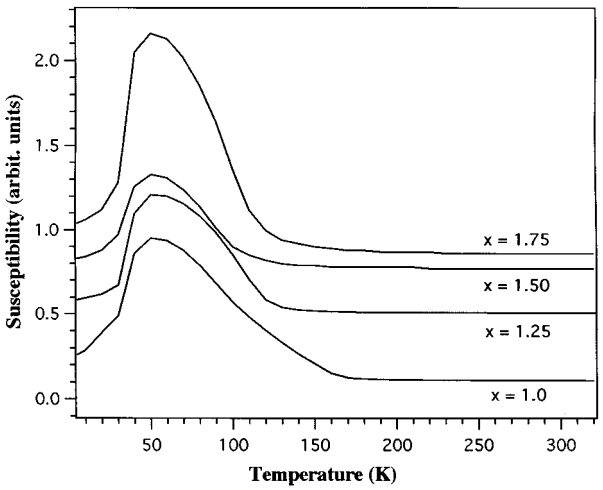

FIG. 8. Zero field cooling susceptibility for $PbFe_xV_{6-x}O_{11}$ for $x = 1, 1.25, 1.5$, and 1.75.

postulated model of the magnetic frustration in the octahedral layers. In the three-dimensional structure, these layers can be considered as clusters of spins that communicate to other clusters through the Fe/V occupancies of the dimeric octahedral and the bipyramidal sites and cause additional frustration. This cluster consideration arises from the characteristic observed shape of the irreversibility between the ZFC and FC branches below T_f in our measurements (23, 27). It is of interest to note that metallic NaV_6O_{11} undergoes a phase transition at 245 K with a change of space group from $P6_3/mmc$ to $P6_3mc$ leading to a slight difference in the lattice constants and therefore to two triangular sublattices (5). However, the two different V(1)–V(1) distances, 2.74601(1) and 2.9589(1) Å, remain within the limits for direct exchange and the compound is ferromagnetic. The χ^{-1} versus T data for PbV_6O_{11} shown in Fig. 5a is concave but presents a linear part above 230 K. It was fit to the Curie–Weiss law and yielded $\mu_{eff} = 4.93$ BM per formula unit instead of the spin-only value of 6.16 BM (0.82 MB/V vs 1.03 BM/V) and $\theta = -80$ K. The negative Weiss constant and the reduced value of the effective moment are consistent with frustration among antiferromagnetic interactions.

Electric Properties

Figure 9 shows the Ln(1/*R*) versus 1000/*T* dependence obtained from measurements on polycrystalline samples of nearly single phase PbV_6O_{11} and single-phase $PbFe_{1.75}V_{4.25}O_{11}$. Both exhibit charge-hopping semiconductor behavior, obeying an Arrhenius law in the investigated temperature range. The break point observed for $PbFe_{1.75}V_{4.25}O_{11}$ is due to the limit of detectibility of the experimental measurement cell. The same saturation value was reached for PbV_6O_{11} at a lower temperature and is not shown on the curve. The activation energies obtained from least-squares refinements are 0.39 and 0.72 eV for PbV_6O_{11} and $PbFe_{1.75}V_{4.25}O_{11}$, respectively. Fe^{3+} substitution for V^{3+} in the framework increases the activation energy for the charge carriers. The V^{4+}/V^{3+} potential is easily accessible for hopping electron or hole transport while Fe^{3+} is very stable to further oxidation to Fe^{4+}. Recent electrochemical measurements performed on mixed Fe/V cathode materials for Li batteries did not allow to reach the Fe^{3+}/Fe^{4+} potential during the Li^+ extraction while V^{3+} oxydation to V^{4+} was observed (28). Thus, the partial or complete occupancy by Fe^{3+} of the $M(2), M(3)$, and $M(4)$ sites is expected to decrease the conductivity parallel to the

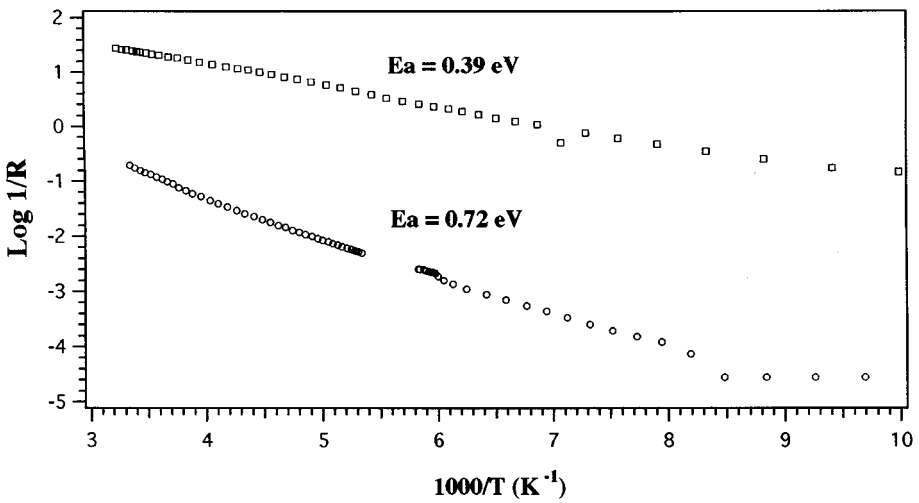

FIG. 9. Log(1/*R*) vs 1000/*T* for PbV_6O_{11} (squares) and $PbFe_{1.75}V_{4.25}O_{11}$ (circles).

c direction and causes E_a to increase with iron substitution. Crystal chemical considerations lead us to suggest that the conductivity in $PbFe_{1.75}V_{4.25}O_{11}$ is essentially two-dimensional and occurs in the a–b plane by the activation of localized electron hopping via short and long bonded pairs of vanadium atoms. In PbV_6O_{11}, however, conductivity should occur in three dimensions. The direct V–V interactions in the a–b plane of NaV_6O_{11} is consistent with its metallic behavior at room temperature (9). In that compound, a semiconductor behavior of the conductivity perpendicular to c occurs from 245 to 80 K, corresponding to the $P6_3mc$ phase and is probably related to the V–V separation into short and long distances as in the lead phases.

Figure 10 shows the Seebeck coefficients α vs T for nearly single-phase PbV_6O_{11} and single-phase $PbFe_{1.75}V_{4.25}O_{11}$. Both curves present the same shape with three peaks at $T \cong 47$, 85, and 120 K. The peaks are distinct in the vanadium phase but appear more rounded in $PbFe_{1.75}V_{4.25}O_{11}$. The coefficient α decreases monotonically after about 130 K and the slope approaches zero at high temperature. Small polaron behavior can be deduced from these curves. It is evidenced by an almost temperature-independent Seebeck coefficient in the high-temperature range because the concentration of carriers is independent of temperature. A standard-band model would give rise to a drastic change of the Seebeck coefficient at high temperature because of the increasing number of thermally activated carriers. For small polaron conduction the Seebeck coefficient is given by

$$\alpha = -k/e \ln \beta - k/e \ln[(1-c)/c] - S_T^0/e,$$

where k is the Boltzman constant, e the electronic charge, β the spin degeneracy factor, c the fraction of conducting sites, and S_T^0 the vibrational entropy associated with the ions surrounding a polaron at a given site (29). Estimates of the latter indicate that it is small enough to be negligible in most cases (30, 31). Thus, α is the sum of a magnetic term and a conductivity term. Because of the complexity of these systems, it is futile to calculate a precise value of the carrier concentration because anisotropic properties of conduction assign different roles to each crystallographic site. Nevertheless, the results allow us to reach the following conclusions:

A. The positive values of α below 300 K for the V-phase and 220 K for the Fe-phase indicate p-type conduction. This is in agreement with the predominant V^{3+} lower oxidation state ratio in both compounds, $V^{3+}/V^{4+} = 2$ and 1.125 for PbV_6O_{11} and $PbFe_{1.75}V_{4.25}O_{11}$, respectively. Conduction arises from the transfer of extra holes present in V^{4+} to the V^{3+} acceptors (32).

B. The three peaks observed in the low-temperature region scale with the ZFC magnetic susceptibility changes. The first peak appearing at 47 K is assigned to the freezing temperature. The second peak, $T \cong 85$ K, corresponds to the decrease of the ZFC susceptibility towards the paramagnetic state. The third peak, $T \cong 120$ K, is attributed to the transition to the paramagnetic behavior. Thus, a close connection between spin frustration and the electrical conduction processes exists. Moreover, the shape of the curve below T_f indicates a transition from semiconductor to insulator. This transition is due to a cessation of carrier hopping below T_f. We were not able to show it by conductivity measurements because the equipment could no longer measure the high resistance.

C. The spin degeneracy is set equal to 1 in a constrained spin system and to 2 in a paramagnetic system. A progressive change of β from 1 to 2 is followed by a 60 μV/K loss in the α value due to the influence on the magnetic term of the

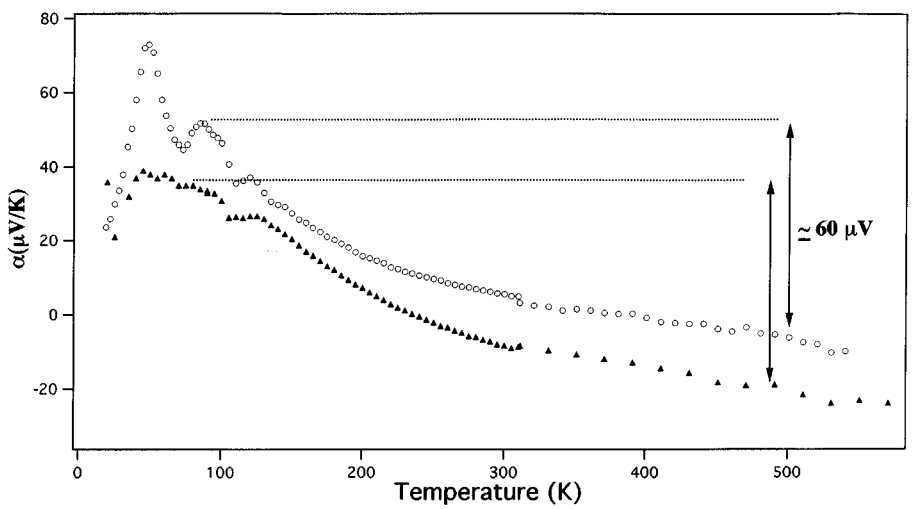

FIG. 10. Seebeck coefficient vs temperature for PbV_6O_{11} (open circles) and $PbFe_{1.75}V_{4.25}O_{11}$ (filled triangles).

α equation. In a spin-glass system it is not possible to estimate the precise temperature at which $\beta = 1$. A good approximation is to choose a temperature between T_f and the transition to paramagnetism. Thus, for both compounds a $\beta = 2$ spin degeneracy sets in at about 500 K. This is in agreement with the low value found for the effective moment calculated for the Currie–Weiss law for PbV_6O_{11}. The compounds exhibit remaining short-range coupling until 500 K. At this point, it is important to note that the change of α from positive to negative values is not due to a conduction type transition of *p* to *n*, but to progressive cancellation of the magnetic exchanges in the system.

D. Finally, the lower values of α for $PbFe_{1.75}V_{4.25}O_{11}$ as compared to PbV_6O_{11} agree with the decrease of carriers in the iron compound, in accord with the conductivity term of the α formula because of the nonparticipation of Fe^{3+} in the conduction process.

CONCLUSION

$PbFe_xV_{6-x}O_{11}$ phases exhibit remarkable electric and magnetic properties that are due to the presence of lead in the cuboctahedral site of the *R* blocks. The presence of the Pb^{2+} lone pair lowers the symmetry from $P6_3/mmc$ to $P6_3mc$. The V(1) atom in the central octahedral layer shifts from the 6(*g*) position (1/2, 0 ,0) in $P6_3/mmc$ and forms V(1) trimers. One trimer has short V–V bond lengths of about 2.7 Å, while the other trimer has a V–V bond about 3.0 Å long. The ferro- and antiferromagnetic exchange coupling within the layer gives rise to frustration and produces a spin glass at low temperatures. The phases are hopping *p*-type semiconductors, in agreement with the predominant V^{3+} cationic presence in the conduction sites. Iron substitution is favored in the triangular bipyramidal *M*(4) sites and occurs partially in the *M*(2) and *M*(3) dimeric sites. A single-phase, solid solution $PbFe_xV_{6-x}O_{11}$ exists in the range $1 \leq x \leq 1.75$. There are two noticeable effects of this substitution. It increases the *c* parameter because of an elongation of the apical Fe^{3+}–O distance of the triangular bipyramid as compared to the V^{4+}–O distance in PbV_6O_{11}. At the same time, Fe^{3+} cations do not participate in the conduction process, inhibiting the electric transport parallel to [001]. Finally, there exists a strong correlation between electric and magnetic properties where the phases change from a *p*-type semiconductor in the paramagnetic region to an insulator in the spin-glass region.

ACKNOWLEDGMENT

Olivier Mentre and Hugo Steinfink acknowledge the support for this research by the R. A. Welch Foundation, Houston, Texas.

REFERENCES

1. O. Mentre and F. Abraham, *J. Solid State Chem.* **125,** 91 (1996).
2. P. B. Moore, P. K. S. Gupta, and Y. Le Page, *Am. Mineral.* **74,** 1186 (1989).
3. X. Obradors, A. Collomb, M. Pernet, D. Samaras, and J. C. Joubert, *J. Solid State Chem.* **56,** 171 (1985).
4. X. Obradors, A. Collomb, J. Pannetier, A. Isalgue, J. Tejada, and J. C. Joubert, *Mat. Res. Bull.* **18,** 1543 (1983).
5. Y. Kanke, F. Izumi, Y. Morii, E. Akiba, S. Funahoshi, K. Kato, M. Isobe, E. Takayama-Muromachi, and Y. Uchida, *J. Solid State Chem.* **112,** 429 (1994).
6. Y. Kanke, K. Kato, E. Takayama-Muromachi, and M. Isobe, *Acta Crystallogr. C* **48,** 1376 (1992).
7. P. Dougier and P. Hagenmuller, *J. Solid State Chem.* **15,** 158 (1975).
8. B. Reuter and K. Muller, *Naturwissenschaften* **54,** 164 (1967).
9. Y. Uchida, Y. Kanke, E. Takayama-Muromachi, and K. Kato, *J. Phys. Soc. Jpn.* **60,** 2530 (1991).
10. Y. Kanke, F. Izumi, E. Takayama-Muromachi, K. Kato, J. Kamiyama, and H. Asano, *J. Solid State Chem.* **92,** 261 (1991).
11. J. De Meulenaer and H. Tompa, *Acta Crystallogr.* **19,** 1014 (1965).
12. "International Tables for X-Ray Crystallography," Vol. IV. Kynoch Press, Birmingham, 1974.
13. D. T. Cromer and D. Liberman, *J. Chem. Phys.* **53,** 1891 (1970).
14. C. T. Prewitt, "SFLS-5, Report ORNL-TM 305." Oak Ridge National Laboratory, Oak Ridge, Tennessee, 1966.
15. M. C. Cadee and D. J. W. Ijdo, *J. Solid State Chem.* **52,** 302 (1984).
16. E. Kneller, M. Velicescu, and F. Haberey, *J. Magn. Magn. Mater.* **7,** 49 (1978).
17. X. Obradors, A. Labarta, A. Isalgue, J. Tejada, J. Rodriguez, and M. Pernet, *Solid State Commun.* **65,** 189 (1988).
18. A. P. Ramirez, G. P. Espinosa, and A. S. Cooper, *Phys. Rev. Lett.* **64,** 2070 (1990).
19. C. Broholm, G. Aeppli, G. P. Espinosa, and A. S. Cooper, *J. Appl. Phys.* **69,** 4968 (1991).
20. X. Obradors, A. Isalgue, A. Collomb, A. Labarta, M. Pernet, J. A. Pereda, J. Tejada, and J. C. Joubert, *J. Phys. Colloq. C* **46,** 339 (1985).
21. G. M. Irwin and E. R. Sanford, *Phys Rev. B* **44,** 4423 (1991).
22. X. Battle, A. Labarta, B. Martinex, X. Obradors, V. Cabanas, and M. Vallet-Regi, *J. Appl. Phys.* **70,** 6172 (1991).
23. B. Martinez, F. Sandiumenge, S. Gali, X. Obradors, and R. Rodriquez-Clemente, *Solid State Commun.* **83,** 649 (1992).
24. A. Manthiram and J. B. Goodenough, *Can. J. Phys.* **65,** 1309 (1987).
25. J. B. Goodenough, "Magnetism and the Chemical Bond." Interscience, New York–London, 1963.
26. K. Moorjani and J. M. D. Coey, "Magnetic Glasses," p. 30. Elsevier, Amsterdam, 1984.
27. J. Hamman, D. Fiorani, M. Yamani, and J. L. Dormann, *J. Phys. C* **19,** 6635 (1986).
28. K. S. Nanjundaswammy, A. K. Padhi, J. B. Goodenough, S. Okada, H. Okada, H. Ohtsuka, H. Arai, and J. Yamaki, *Solid State Ionics*, accepted for publication.
29. H. L. Tuller and A. S. Nowick, *J. Phys. Chem. Solids* **38,** 859 (1977).
30. I. G. Austin and N. F. Mott, *Adv. Phys.* **18,** 41 (1969).
31. J. B. Goodenough, *Mater. Res. Bull.* **5,** 621 (1970).
32. P. A. Cox, "Transition Metal Oxides," p. 166. Clarendon Press, Oxford, 1995.